

---

# Sample-efficient image segmentation through recurrence

---

Drew Linsley<sup>†</sup>      Junkyung Kim<sup>†</sup>      Thomas Serre  
Carney Institute for Brain Science  
Department of Cognitive Linguistic & Psychological Sciences  
Brown University  
Providence, RI 02912  
{drew\_linsley, junkyung\_kim, thomas\_serre}@brown.edu

## Abstract

There is a growing consensus in vision science that recurrent neural networks constitute better models of visual cortex than feedforward architectures. Yet, feedforward neural networks continue to dominate the leaderboards for most popular computer vision challenges. We bridge this gap with the  $\gamma$ -Net. Inspired by recurrent feedback loops prevalent in the mammalian visual cortex,  $\gamma$ -Net introduces gated recurrent dynamics through feedforward, horizontal, and top-down connections into the popular U-Net architecture. We demonstrate that  $\gamma$ -Net performs on par or better than state-of-the-art architectures for dense prediction in both natural image and cell segmentation datasets. The re-entrant processing of the  $\gamma$ -Net lead to especially large performance gains over the state-of-the-art on smaller datasets. We further show that  $\gamma$ -Net reproduces a contextual bias in orientation estimation which is consistent with the tilt illusion in human psychophysics. The existence of this bias in  $\gamma$ -Net – which emerges from contour detection training in natural images – supports the theory that this visual illusion is a byproduct of recurrent computational mechanisms underlying contour detection. Vision science theory suggests that recurrent processing underlies robust biological vision, and we demonstrate that similar principles can improve the data efficiency of computer vision systems.

## 1 Introduction

Convolutional neural networks (CNNs) are often considered the *de facto* “standard model” of vision. CNNs and their extensions represent the state of the art for most computer vision applications with performance approaching – and sometimes exceeding – that of human observers on certain visual recognition tasks [1–3]. They have also been shown to provide the best fit to rapid neural responses in the visual cortex (see [4, 5] for reviews). However, multiple lines of evidence also suggest that CNNs are outmatched by the power and versatility of the visual brain. For example, CNNs suffer from occlusions and clutter [6–8]. CNNs are also limited in their ability to learn visual relations [9], solve simple incremental grouping tasks [10], and generalize between image datasets [11]. Most importantly, state-of-the-art CNNs are heavily overparameterized and require massive datasets to reach their impressive accuracy [12].

Neuroscience has long suggested that cortical feedback is central to biological vision’s great versatility and robustness [13–15]. Feedforward projections in the visual system are almost always matched by feedback projections [16]. A widely held assumption is that operations implemented through

---

<sup>†</sup>These authors contributed equally to this work.

feedback leverage context to iteratively refine feedforward visual representation when stimuli are ambiguous, degraded or occluded [17, 18]. Consistent with this view, recent studies have found that the dynamic interactions between feedforward and feedback signals in the visual cortex can be better accounted for by recurrent neural networks (RNNs) than feedforward networks [6, 8, 19–22]. Despite a growing number of attempts to incorporate feedback operations into computer vision systems [8, 10, 18, 21–26], common benchmarks are still dominated by CNNs that rely only on feedforward operations. We suspect that this is because CNNs leverage large-scale datasets to learn operations that are otherwise more efficiently implemented through feedback. We hypothesize that recurrent feedback will have its greatest impact on computer vision applications that require generalization from small training datasets – scenarios where feedforward CNNs can easily overfit.

We introduce  $\gamma$ -Net, a highly recurrent extension of the U-Net [27], which outperforms state-of-the-art CNN models for dense prediction of image contours. We extend the hGRU of Linsley et al. [10], which was designed for learning horizontal connections between neighboring units within a layer, to incorporate a broader and more general form of feedback that includes top-down connections from higher to lower processing stages. We evaluate our proposed  $\gamma$ -Net on two representative contour detection problems: neuron segmentation in high-resolution serial electron microscope (SEM) images [28, 29] and object contour detection in natural images [30]. Our results show that  $\gamma$ -Net performs on par or better than state-of-the-art contour detection models while achieving far better training sample efficiency, demonstrating a key function for feedback in computer vision. Additionally, we found that our proposed recurrent architecture, when trained to detect contours in natural images, reproduces a similar visual illusion in orientation estimation as human observers.

**Contributions** (i) a novel highly-recurrent extension of the U-Net which is (ii) systematically evaluated on multiple contour detection problems, (iii) performs on par or better than the state of the art with reduced sample complexity and (iv) reproduces a contextual visual illusion exhibited by humans. Our work provides compelling evidence that the inclusion of recurrent circuits in CNNs yields more sample-efficient network models that are also more consistent with biology.

## 2 Related work

In contrast to CNNs, which build processing depth through a cascade of filtering and pooling stages, RNNs can learn to dynamically process stimuli by re-using filtering operations over “timesteps” of recurrence. RNNs were originally developed to process temporal sequences (e.g., [31]), but have been extended to static images. Notable efforts in this line of work are multi-dimensional RNNs [32], which treat images as pixel sequences, and convolutional-RNNs, which learn spatial kernels to compute RNN activities. There are now many successful applications of RNNs in computer vision, including object recognition and super-resolution tasks [26, 33, 34]. Others have shown the benefits of introducing learning rules or connectivity patterns that are inspired by the anatomy and/or the physiology of the visual cortex into RNNs [21, 24, 35–37].

In the current work, we take inspiration from such connectivity patterns in designing the  $\gamma$ -Net. We are motivated by the horizontal gated recurrent unit (hGRU) [37], which approximates a recurrent neural circuit model of a variety of contextual phenomena in cortex [38]. The hGRU is able to learn this approximation by utilizing a gated convolutional-RNN module [39], giving it the ability to learn “horizontal connections” between units separated by spatial location and feature channels. A single layer of this hGRU module learned long-range spatial dependencies for a contour integration task that CNNs with orders-of-magnitude more weights could not. As we describe below, we extend this hGRU module into a more general-purpose “feedback” gated recurrent unit (fGRU) that can learn either horizontal connections (between units in a layer) or top-down connections (from units in a higher layer to units in a lower layer).

Several RNN-based models have been developed for cell segmentation in Serial Electron Microscope (SEM) images for connectomics. These models build off of the U-Net architecture, and can be roughly be grouped as those which (i) add timesteps of recurrence at individual layers [40] or (ii) introduce top-down (but not horizontal, as in [37]) feedback by re-processing the stimulus multiple times through the same architecture [41–43]. The  $\gamma$ -Net distinguishes itself from these implementations in two ways. Unlike the first approach, recurrence is not isolated at the level of individual layers: the activity of every recurrent unit in the  $\gamma$ -Net is a function of other recurrent units both within the same layer and in different layers. Unlike models in the second approach, which use 1 [42], 2 [41], or 3

[43] timesteps of recurrent processing, the  $\gamma$ -Net maintains recurrent connections at every layer over 8 timesteps. While using shorter recurrent timesteps might be preferred in these architectures for better trainability, we found that our  $\gamma$ -Net architecture is not adversely affected by longer processing timesteps, partially thanks to the extensive use of learned gates [37] (see SI for details).

### 3 $\gamma$ -Net

The  $\gamma$ -Net builds on the popular U-Net architecture [27] with two forms of recurrent connections: horizontal connections between units within a layer, and top-down connections extending from higher-level units onto lower-level units. Both architectures are depicted in Fig. 1. A standard U-Net can be traced by following information flow through the black “feedforward” connections in the diagram. It makes per-pixel predictions by passing the input through a series of down-sampling transformations (filtering, pooling, and subsampling), which are followed by a series of up-sampling transformations (transpose convolution and filtering), and “skip” connections that mix information in down- and up-sampling layers of the same spatial resolution. The U-Net achieves processing depth by introducing more layers in the downsampling and upsampling paths. For example, the U-Net we use in our experiments has a depth of  $\ell = 5$ , which enabled it to achieve “superhuman” cell segmentation performance (see SI for a diagram of this model and details on its implementation; [2]).

The  $\gamma$ -Net architecture can also be viewed in Fig. 1 by following the diagram’s black feedforward connections to the red recurrent connections. Similar to the U-Net of [2], it uses a simple down- and up-sampling pathway with depth of  $\ell = 5$ . However, unlike the U-Net,  $\gamma$ -Net introduces two forms of recurrent connections between these pathways. These are “horizontal” connections, which recurrently spread information between computational units within a layer, and “top-down” connections, which allow units in a downstream layer (e.g., second layer) to influence units in an upstream layer (e.g., first layer). In every timestep of recurrent processing (for a total of  $\tau$  steps), the  $\gamma$ -Net executes a “bottom-up” followed by a “top-down” pass of information through all of its layers (akin to repeated cycles of the information flow through a standard U-Net), in which the activity of every recurrent unit becomes a highly nonlinear function of every other unit. Thus,  $\ell$  and  $\tau$  are complementary hyperparameters for increasing the processing depth of the  $\gamma$ -Net, with the latter having the advantage of not introducing additional parameters.

The recurrent dynamics of the  $\gamma$ -Net are inspired by the horizontal Gated Recurrent Unit (hGRU) module, a biologically-inspired RNN module for learning horizontal connections between units in a convolutional layer, that was found to be especially effective for contour integration [10]. We begin by reviewing a formulation of the hGRU.

The equations below describe the evolution of recurrent units in  $\mathbf{H} \in \mathbb{R}^{W \times H \times K}$ , which are influenced by the non-negative feedforward drive  $\mathbf{X} \in \mathbb{R}^{W \times H \times K}$  (i.e., a convolutional layer response to a stimulus) over discrete timesteps, denoted by  $\cdot[t]$ . For clarity, we bold tensors to distinguish them from learned kernels and parameters:

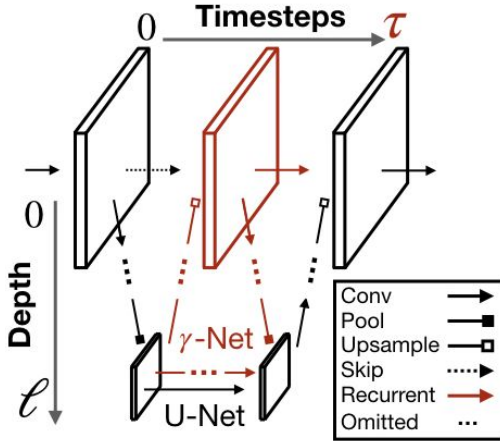


Figure 1:  $\gamma$ -Net is a highly-recurrent extension of U-Net designed for dense image prediction tasks. Here, a U-Net and  $\gamma$ -Net architecture are depicted together. Black “feedforward” connections denote operations for transforming an image into a per-pixel prediction through a series of down- and up-sampling operations. “Skip-connections” merge activities in the up-sampling pathway with those in the down-sampling pathway of identical spatial resolution. The  $\gamma$ -Net extends introduces recurrent connections that implement a bottom-up to top-down information flow that resembles a  $\gamma$ . Its path of information flow can be traced by following the black feedforward connections to the red “recurrent” connections.  $\gamma$ -Net expressiveness is a function of depth,  $\ell$ , and recurrent timesteps,  $\tau$ .

$$\begin{aligned}
\mathbf{G}^I &= \text{sigmoid}(U^I * \mathbf{H}[t-1]) \\
\mathbf{C}^I &= W^I * (\mathbf{H}[t-1] \odot \mathbf{G}^I) \\
\mathbf{Z} &= \left[ \mathbf{X} - \left[ (\alpha \mathbf{H}[t-1] + \mu) \mathbf{C}^I \right]_+ \right]_+ \\
\mathbf{G}^E &= \text{sigmoid}(U^E * \mathbf{Z}) \\
\mathbf{C}^E &= W^E * \mathbf{Z} \\
\tilde{\mathbf{H}} &= \left[ \kappa(\mathbf{C}^E + \mathbf{Z}) + \omega(\mathbf{C}^E * \mathbf{Z}) \right]_+ \\
\mathbf{H}[t] &= (1 - \mathbf{G}^E) \odot \mathbf{H}[t-1] + \mathbf{G}^E \odot \tilde{\mathbf{H}}
\end{aligned} \tag{1}$$

The model consists of two stages: first,  $\mathbf{X}$  is inhibited by horizontal interactions between units in  $\mathbf{H}[t-1]$  to produce the intermediate activity  $\mathbf{Z}$ . Second,  $\mathbf{H}$  is updated with excitatory horizontal interactions between units in  $\mathbf{Z}$ . Recurrently repeating these two operations enables the module to perform a combination of digital selection and analog amplification of task-relevant features [44].

In the first stage, activity of  $\mathbf{H}[t-1]$  (i.e., from a previous timestep) is modulated by the gate  $\mathbf{G}^I$ . This gate activity is computed by applying the sigmoid nonlinearity to a convolution of the kernel  $U^I \in \mathbb{R}^{1 \times 1 \times K \times K}$  with  $\mathbf{H}$ . At the same time, horizontal inhibitory interactions are computed with the kernel  $W^I \in \mathbb{R}^{S \times S \times K \times K}$ , where  $S$  describes the spatial extent of horizontal connections on a single timestep (see SI for details on how this is set in  $\gamma$ -Nets). This kernel  $W^I$  is convolved with an element-wise product of the gate  $\mathbf{G}^I$  and  $\mathbf{H}[t-1]$ . The intermediate  $\mathbf{Z}$  is computed by inhibiting the feedforward drive with linear and multiplicative combinations of  $\mathbf{H}[t-1]$  and  $\mathbf{C}^I$ , controlled by the parameters  $\mu, \alpha \in \mathbb{R}^K$ . Positive rectification is denoted by  $[\cdot]_+$  and non-negativity is enforced in  $\mathbf{Z}$ .

In the second stage,  $\mathbf{Z}$  is separately convolved with the kernels  $W^E \in \mathbb{R}^{S \times S \times K \times K}$  and  $U^E \in \mathbb{R}^{1 \times 1 \times K \times K}$  to compute excitatory horizontal interactions  $\mathbf{C}^E$  and the activity of  $\mathbf{G}^E$ , a gate for updating the persistent hidden state. Additive and multiplicative forms of excitation are scaled by the parameters  $\kappa, \omega \in \mathbb{R}^K$ , and  $\mathbf{H}[t-1]$  is interpolated with the candidate activity  $\tilde{\mathbf{H}}$  to compute  $\mathbf{H}[t]$ .

We extend this hGRU module into a general-purpose feedback gated recurrent unit (fGRU) by relaxing constraints on the origins of its feedforward drive  $\mathbf{X}$  and its persistent output activity  $\tilde{\mathbf{H}}$ . Consider the recurrent activities at two layers in the  $\gamma$ -Net of Fig. 1, which we denote  $\mathbf{H}^{(l)}[t]$  and  $\mathbf{H}^{(l+1)}[t]$ . We define a function fGRU, which mixes their hidden states with the dynamics in Eq. 1:  $\mathbf{H}^{(l)}[t] = \text{fGRU}(\mathbf{H}^{(l)}[t], \mathbf{H}^{(l+1)}[t])$ . The updated  $\mathbf{H}^{(l)}$  has been inhibited by activity in  $\mathbf{H}^{(l+1)}$ , and then excited by a learned kernel. We have now defined the fGRU for learning either horizontal or top-down connections. Note that only in the former case – when learning horizontal connections – does the fGRU incorporate persistent activity (see SI for implementation details).

## 4 Experiments

We evaluated  $\gamma$ -Net performance for dense image prediction on two distinct and popular boundary detection tasks: cell membrane detection in serial electron microscopy (SEM) images, and object contour detection in natural images. As discussed in the SI, we optimized our  $\gamma$ -Net architecture on synthetic cell datasets, which we used to systematically compare the performance of different model configurations without overfitting to either of the main contour detection datasets. The  $\gamma$ -Net configurations used on both datasets are parameterized slightly differently, to better resemble state-of-the-art approaches. However, both versions use 8-timesteps of recurrence and instance normalization to minimize the vanishing gradient problem [45, 46]. Model losses are calculated with their final timestep of activity, to promote highly nonlinear model dynamics, and models were trained with single-image batches and the Adam optimizer [47]. Experiments were run in Tensorflow with NVIDIA Titan RTX GPUs.

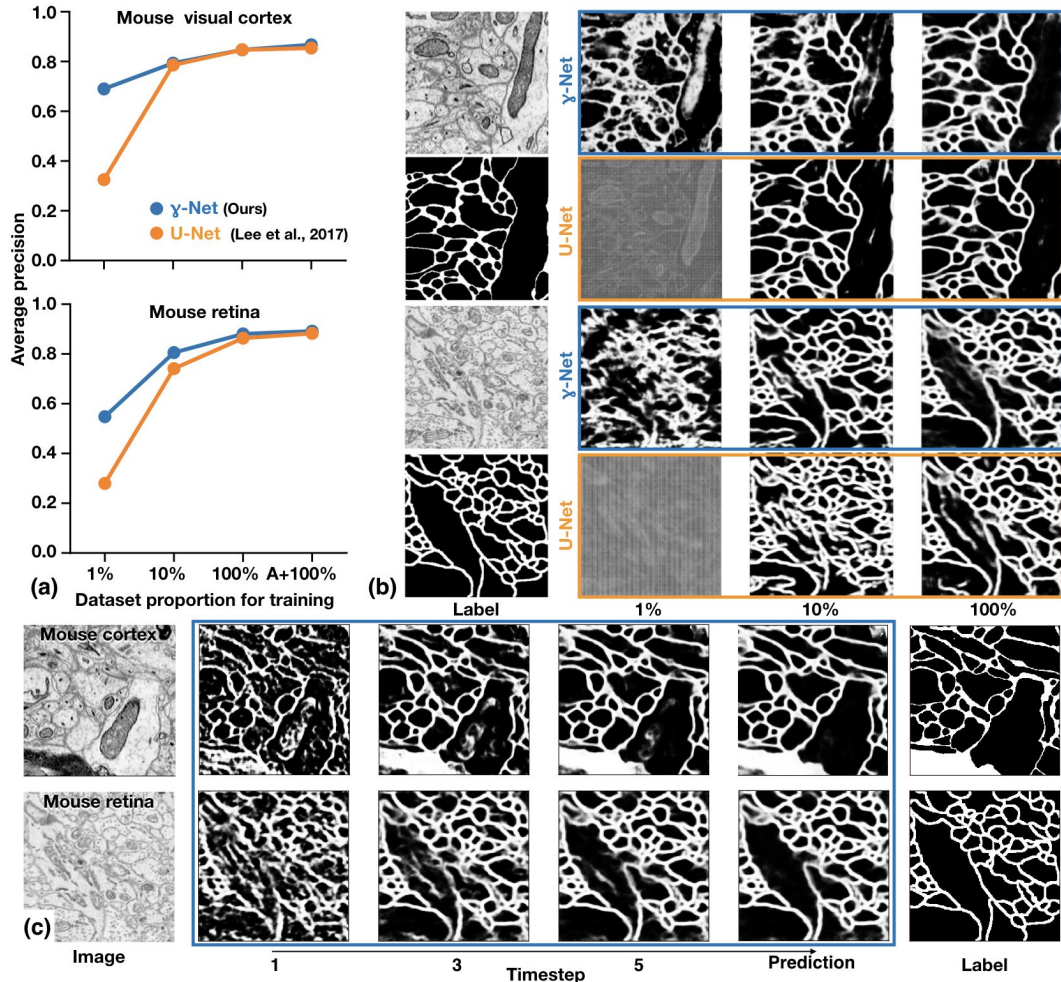


Figure 2: Membrane prediction in SEM images of neural tissue. (a) The  $\gamma$ -Net performs on par or better than a state-of-the-art U-Net [2] for membrane detection when trained on any proportion of the separate SEM image datasets depicting mouse visual cortex or retina tissue. Performance is the mean of per-slice average precision (see SI for model validations with a segmentation metric). The greatest difference in performance between the models was observed after training on 1% of each dataset. (b) Network predictions after training on different proportions of each dataset. (c) Visualizing the evolution of  $\gamma$ -Net predictions across timesteps of processing. Recurrent processing iteratively suppresses contours belonging to internal cell features, such as organelles.

#### 4.1 Cell segmentation

Mapping the connections between neurons in the brain is an important step towards understanding the algorithms that neurons implement. CNNs are used to automate this task by detecting neuron membranes in every pixel/voxel of high-resolution SEM images. Progress towards automation has been driven by challenges like SNEMI3D [28], which contains annotated images of mouse cortex.

The current state-of-the-art in SNEMI3D is a variant of the popular U-Net architecture [27], which uses a different depth, different number of feature maps at every layer, and introduces additional operations such as residual connections [2]. We developed a  $\gamma$ -Net for cell membrane segmentation that incorporates recurrent connections into a modification of this U-Net model. The  $\gamma$ -Net contains five down-sampling blocks (convolution, pooling and subsampling), and four up-sampling blocks (transpose convolution and convolution). In contrast to the U-Net of Lee et al. [2], the  $\gamma$ -Net replaces the convolutional residual layers within each of these blocks with a single layer of convolution followed by an fGRU. In the down-sampling pathway, these fGRUs learn horizontal connections



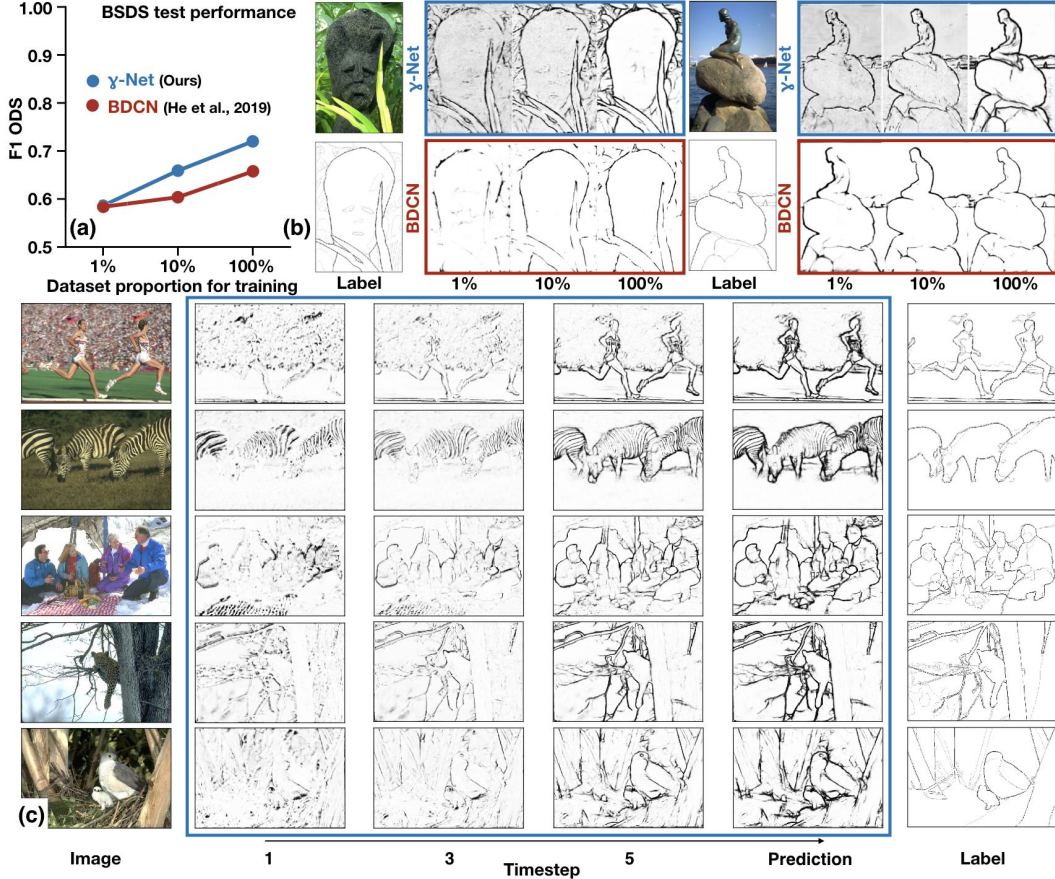


Figure 3: Contour detection in natural images. Models were trained to detect object contours in BSDS500 images. (a) The  $\gamma$ -Net performs on par or better than the state-of-the-art network for contour detection (BDCN; [48]) when trained on 1%, 10%, or 100% of the dataset. Performance is reported as F1 ODS as in [49]. (b) Model predictions after training on the different proportions of BSDS500 images. (c) The evolution of  $\gamma$ -Net predictions across timesteps of processing. Initially coarse detections are refined over processing timesteps to select figural object contours.

between spatially neighboring units in the preceding convolutional layer. In the up-sampling pathway, the fGRUs learn top-down connections between persistent activities of high- and low-level layers. Similar to [2], transpose convolutions match the spatial and channel dimensions of activities between successive layers. The model’s final prediction is linearly read-out from the first fGRU layer, which maintains a representation of the same height and width as the input image. The  $\gamma$ -Net was trained from a random initialization using back-propagation through time (BPTT), and we found that its gradient stability was improved by introducing a persistent activity for feedforward units in its down-sampling and up-sampling layers. This, in effect, is equivalent to residual connections between timesteps and was implemented with a minimal gated unit variant [50], which learned to interpolate between unit activity before and after each recurrent update (see SI for a full model description). We systematically compared different parameterizations of the  $\gamma$ -Net on a separate dataset of synthetic cell images, in which we found clear benefits for the fGRU over other recurrent models, along with maximizing timesteps of recurrent processing (see SI for details).

We began by measuring model accuracy for membrane detection in images from the SNEMI3D challenge. We first split the dataset into training (80 slices) and test sets (20 slices) and followed the training routine of [2] to validate our implementation of their U-Net (see SI, where we demonstrate similar super-human segmentation performance). Next, we generated versions of the dataset containing 1%, 10%, or 100% of the training set, as well as a version of the full training set augmented with random left-right and up-down flips (A+100%). Models were trained to minimize class-balanced bi-

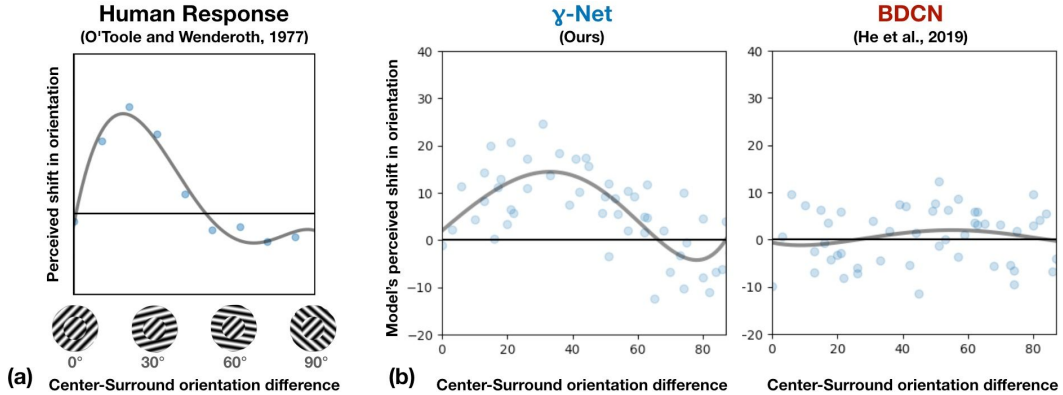


Figure 4: The  $\gamma$ -Net reproduces a contour detection illusion exhibited by human observers. (a) The orientation-tilt illusion [51] emerges in the perception of the orientation of a center grating as the orientation of its surround changes. Perception of the center orientation is repulsed from the surround when the two are in similar orientations (e.g.,  $\approx 30\text{deg}$ ), and attracted to the surround when the two are in dissimilar but not orthogonal orientations (e.g.,  $\approx 60\text{deg}$ ). (b) We investigated the presence of such an illusion in models trained on contour detection in natural images. Model weights were fixed and readouts were added to each and trained to decode the orientation of grating stimuli in which the center and surround orientations were the same. Next, the models were tested on grating stimuli in which surround orientations were systematically varied w.r.t. the center (exemplars depicted in panel a). The  $\gamma$ -Net but not the BDCN demonstrated a bias in decoding grating orientation that coincided with humans, displaying both repulsion and attraction. Gray curves depict a fourth-order polynomial fit.

nary cross-entropy for 500 epochs with the Adam optimizer and a learning rate of  $1e^{-2}$ . Performance was taken as the mean of average precisions across the test image set.

The  $\gamma$ -Net exceeded 0.60 average precision when trained on only 1% of the dataset (Fig. 2a). By comparison, the U-Net needed at least 10% of the dataset to exceed this mark. The performance of both models monotonically increased with additional data. We validated this pattern of results on a separate cell image dataset of mouse retina (384 slices total; 307 for training and the rest for testing; see SI for details). Using the same training routines, we again found that  $\gamma$ -Net performance exceeded the U-Net when trained on 1% of this dataset (Fig. 2b). While the performance of both models again monotonically increased with additional data, the  $\gamma$ -Net held a slight advantage over the U-Net in each case (Fig. 2a).

The strong performance of the  $\gamma$ -Net in membrane detection suggests that its recurrent circuits are helpful for cell membrane detection, but does not guarantee that the model uses recurrence in a nontrivial way. We investigated how the  $\gamma$ -Net uses recurrent processing for membrane detection by visualizing activity at every timestep of the  $\gamma$ -Net trained on the A+100% dataset. Membrane predictions were obtained by passing neural activity at every timestep through the final linear readout. This revealed that the  $\gamma$ -Net learns a complex visual strategy for membrane detection: it gathers a coarse “gist” of membranes in the first timestep of processing, and iteratively refines these predictions by clearing out spurious contours for elements like cell organelles while also enhancing cell boundaries (Fig. 2c). Similar strategies were observed on both cell image datasets.

## 4.2 Contour detection in natural images

The BSDS500 dataset is a classic dataset for testing contour detection algorithms in natural images. It contains object-boundary annotations for 500 images, which are split into train (200), validation (100), and test (200) sets. Because of its small size, leading approaches to the BSDS500 begin with a CNN trained on ILSVRC12 object recognition, and then fine-tune additional components for contour detection. The current leading approach is the Bi-Directional Cascade Network (BDCN) [48], which places multi-layer readouts at every processing block in a pretrained VGG16, and uses a loss that combines these readouts to balance their contribution on the final prediction.

Our  $\gamma$ -Net for BSDS500 also begins with a ILSVRC12-pretrained VGG16, which functions as its feedforward/down-sampling “backbone”. We introduce fGRU modules into this architecture for learning horizontal and top-down connections between units in the final convolutional layers of the second through fifth VGG16 convolutional blocks. Bilinear resize operations and  $1 \times 1$  convolutions were used to pass top-down activities between layers (see SI for architecture details). In contrast to the BDCN (and other recent approaches to BSDS), we only readout from the first fGRU in the  $\gamma$ -Net (which is closest to the resolution of the input image), since we expected that the model’s horizontal and top-down connections would enable it to combine information between layers – and thus scales – if necessary. The model is trained to minimize the weighted binary cross-entropy [48] between this layer’s prediction and contour labels.

Do recurrent feedback connections help to learn natural contour segmentation? We investigated this question by training the  $\gamma$ -Net and BDCN on 1%, 10%, and 100% of the BSDS500 dataset (without augmentations), and evaluating model performance as F1 ODS [49] on the BSDS500 test set. We used a BDCN implementation released by the authors, and trained it using the training routine described in [48] (including learning rates, regularization, batch size, and optimizer; we also confirmed that this model reached published performance on the full BSDS). The  $\gamma$ -Net was trained with the Adam optimizer and learning rates of  $3e^{-4}$  on its randomly initialized fGRU weights and  $1e^{-5}$  on its VGG-initialized weights. We measured performance on the BSDS500 validation set and selected the top-performing model weights for evaluation (model training routines are detailed in the SI).

We found that the  $\gamma$ -Net performed on par or better than the BDCN on each partition of the training dataset. When trained with 1% of the data, performance was similar, but the  $\gamma$ -Net outperformed the BDCN by 10% when trained on either 10% or 100% of BSDS500 (Fig. 3a; see 3b for predictions by both models). In fact,  $\gamma$ -Net performance after training on 10% of BSDS500 was equivalent to BDCN performance after training on 100% of the images.

We again investigated the recurrent feedback strategies learned by  $\gamma$ -Net for detecting contours in natural images. Visualizing model performance on every timestep demonstrated a similar strategy of iterative refinement as we found with cell membrane detection. For example, the top row of Fig. 3b shows that it takes longer for the model to selectively enhance the boundaries around the runner’s bodies while suppressing the feature activities created by the crowd in the background by essentially treating it as a single textured region. In the next row of predictions, it is apparent that the model’s initial zebra-stripe detections are gradually undone and overtaken by its selection of body contours.

### 4.3 Human psychophysics

The recurrent strategies used by the  $\gamma$ -Net for contour detection are qualitatively similar to those described in visual neuroscience (see [52] for review). To what extent does the model also match human psychophysics data? The orientation-tilt illusion is a well-studied phenomenon of human perception [51], in which the orientation of a center grating is biased by the orientation of its surround (Fig. 4a). When the two are oriented similarly, perception of the center orientation tilts away from the surround. When the two are oriented differently, perception of the center orientation is tilted towards the surround. This illusion has been attributed to recurrent dynamics implemented by visual cortex, and speculated to reflect inductive biases for contour integration in the visual cortex [53]. We tested this theory by training an orientation classifier on the output of our  $\gamma$ -Net trained on the full BSDS500 dataset. This classifier was trained on a dataset of full image grating stimuli (i.e., the center and surround orientations were the same), and consisted of two  $1 \times 1$  convolution layers and an intervening linear rectification to map model activities into the sine and cosine of grating orientation. We trained the readout decoder using 100K training images that spanned all orientations and spatial frequencies of gratings. Both the  $\gamma$ -Net and BDCN achieved nearly perfect performance on a held-out validation set of gratings.

We tested the model on 1K test grating stimuli generated with similar properties as those described in [51], and recorded network responses to the center pixel (see SI for details). Surprisingly, the  $\gamma$ -Net encodings of these test images reproduced a qualitatively similar tilt illusion as found in human perceptual data (Fig. 4b). It demonstrated no orientation bias when the surround orientation was equal to the center (as was found in the training dataset of grating images). However, the model’s estimated orientation of the center grating tilted away from the surround as the difference between center-surround orientations increased. As this difference approached 90 degrees, the model’s estimated



orientation of the center grating was tilted towards the surround. Note that this effect cannot be predicted by accidental factors such as aliasing between the center and the surround, which would predict the opposite pattern from the one we observe. Indeed, the BDCN which relies on feedforward operations to detect contours did not exhibit the same illusion.

## 5 Conclusion

One of the key issues in deep learning is that modern architectures are heavily over-parameterized and require very large datasets for training. Our  $\gamma$ -Net architecture leverages both horizontal (within a layer) and top-down (from higher onto lower layers) feedback connections to learn dense image prediction tasks from far fewer examples than purely feedforward architectures.

Feedback has long been suspected as critical for efficiently executing complex visual routines [52]. While this has been demonstrated on synthetic, toy datasets [37], here we demonstrate that feedback also yields efficient performance in complex image datasets. Consistent with theory on feedback routines [52], the  $\gamma$ -Net learns to solve these tasks by iteratively refine a coarse over-segmented prediction. It also exhibits a similar contour detection bias as human vision. Overall, our results demonstrate that feedback models are viable for competing with state-of-the-art feedforward architectures, and may hold great potential as models for biological vision.

## Acknowledgments

This work was funded by ONR grant #N00014-19-1-2029 and the ANR-3IA Artificial and Natural Intelligence Toulouse Institute. This work was also made possible by hardware resources made available by Google (via the TensorFlow Research Cloud (TFRC) program) as well as Meridian IT and IBM. Additional support provided by the Carney Institute for Brain Science and the Initiative for Computation in Brain and Mind at Brown University, the Center for Vision Research (CVR) and the Center for Computation and Visualization (CCV). TS serves as a scientific advisor for Vium Inc, which may potentially benefit from the research results.

## References

- [1] K. He, X. Zhang, S. Ren, and J. Sun. Deep residual learning for image recognition. In *Proceedings of the IEEE conference on computer vision and pattern recognition*, pages 770–778, 2016.
- [2] K. Lee, J. Zung, P. Li, V. Jain, and H. Sebastian Seung. Superhuman accuracy on the SNEMI3D connectomics challenge. In *Neural Information Processing Systems*, 2017.
- [3] P. J. Phillips, A. N. Yates, Y. Hu, C. A. Hahn, E. Noyes, K. Jackson, J. G. Cavazos, G. Jeckeln, R. Ranjan, S. Sankaranarayanan, J.-C. Chen, C. D. Castillo, R. Chellappa, D. White, and A. J. O’Toole. Face recognition accuracy of forensic examiners, superrecognizers, and face recognition algorithms. *Proc. Natl. Acad. Sci. U. S. A.*, 115(24):6171–6176, June 2018.
- [4] N. Kriegeskorte. Deep neural networks: A new framework for modeling biological vision and brain information processing. *Annu Rev Vis Sci*, 1:417–446, November 2015.
- [5] D. L. K. Yamins and J. J. DiCarlo. Using goal-driven deep learning models to understand sensory cortex. *Nat. Neurosci.*, 19(3):356–365, February 2016.
- [6] A. M. Fyall, Y. El-Shamayleh, H. Choi, E. Shea-Brown, and A. Pasupathy. Dynamic representation of partially occluded objects in primate prefrontal and visual cortex. *Elife*, 6, September 2017.
- [7] A. Rosenfeld, R. Zemel, and J. K. Tsotsos. The elephant in the room. August 2018.
- [8] H. Tang, M. Schrimpf, W. Lotter, C. Moerman, A. Paredes, J. Ortega Caro, W. Hardesty, D. Cox, and G. Kreiman. Recurrent computations for visual pattern completion. *Proc. Natl. Acad. Sci. U. S. A.*, 115(35):8835–8840, August 2018.

- [9] J. K. Kim, M. Ricci, and T. Serre. Not-So-CLEVR: learning same–different relations strains feedforward neural networks. *Interface Focus theme issue on “Understanding images in biological and computer vision”*, 2018.
- [10] D. Linsley, J. Kim, V. Veerabadrán, C. Windolf, and T. Serre. Learning long-range spatial dependencies with horizontal gated recurrent units. In S. Bengio, H. Wallach, H. Larochelle, K. Grauman, N. Cesa-Bianchi, and R. Garnett, editors, *Advances in Neural Information Processing Systems 31*, pages 152–164. Curran Associates, Inc., 2018.
- [11] B. Recht, R. Roelofs, L. Schmidt, and V. Shankar. Do CIFAR-10 classifiers generalize to CIFAR-10? June 2018.
- [12] B. M. Lake, R. Salakhutdinov, and J. B. Tenenbaum. Human-level concept learning through probabilistic program induction. *Science*, 350(6266):1332–1338, December 2015.
- [13] S. Hochstein and M. Ahissar. View from the top: Hierarchies and reverse hierarchies in the visual system. *Neuron*, 36(5):791–804, 2002.
- [14] D. Wyatte, D. J. Jilk, and R. C. O’Reilly. Early recurrent feedback facilitates visual object recognition under challenging conditions. *Front. Psychol.*, 5:674, July 2014.
- [15] H. Kafaligonul, B. G. Breitmeyer, and H. Ögmen. Feedforward and feedback processes in vision. *Front. Psychol.*, 6:279, March 2015.
- [16] D. J. Felleman and D. C. Van Essen. Distributed hierarchical processing in the primate cerebral cortex. *Cereb. Cortex*, 1(1):1–47, 1991.
- [17] R. C. O’Reilly, D. Wyatte, S. Herd, B. Mingus, and D. J. Jilk. Recurrent processing during object recognition. *Front. Psychol.*, 4(April):1–14, 2013.
- [18] C. J. Sporer, P. McClure, and N. Kriegeskorte. Recurrent convolutional neural networks: A better model of biological object recognition. *Front. Psychol.*, 8:1551, September 2017.
- [19] P. C. Klink, B. Dagnino, M.-A. Gariel-Mathis, and P. R. Roelfsema. Distinct feedforward and feedback effects of microstimulation in visual cortex reveal neural mechanisms of texture segregation. *Neuron*, June 2017.
- [20] M. Siegel, T. J. Buschman, and E. K. Miller. Cortical information flow during flexible sensorimotor decisions. *Science*, 348(6241):1352–1355, June 2015.
- [21] A. Nayebi, D. Bear, J. Kubilius, K. Kar, S. Ganguli, D. Sussillo, J. J. DiCarlo, and D. L. Yamins. Task-Driven convolutional recurrent models of the visual system. In S. Bengio, H. Wallach, H. Larochelle, K. Grauman, N. Cesa-Bianchi, and R. Garnett, editors, *Advances in Neural Information Processing Systems 31*, pages 5295–5306. Curran Associates, Inc., 2018.
- [22] K. Kar, J. Kubilius, K. Schmidt, E. B. Issa, and J. J. DiCarlo. Evidence that recurrent circuits are critical to the ventral stream’s execution of core object recognition behavior. *Nat. Neurosci.*, April 2019.
- [23] D. George, W. Leirach, K. Kansky, M. Lázaro-Gredilla, C. Laan, B. Marthi, X. Lou, Z. Meng, Y. Liu, H. Wang, A. Lavin, and D. S. Phoenix. A generative vision model that trains with high data efficiency and breaks text-based CAPTCHAs. *Science*, 358(6368), December 2017.
- [24] W. Lotter, G. Kreiman, and D. Cox. Deep predictive coding networks for video prediction and unsupervised learning. May 2016.
- [25] H. Wen, K. Han, J. Shi, Y. Zhang, E. Culurciello, and Z. Liu. Deep predictive coding network for object recognition. February 2018.
- [26] Q. Liao and T. Poggio. Bridging the gaps between residual learning, recurrent neural networks and visual cortex. April 2016.
- [27] O. Ronneberger, P. Fischer, and T. Brox. U-Net: Convolutional networks for biomedical image segmentation. May 2015.

- [28] N. Kasthuri, K. J. Hayworth, D. R. Berger, R. L. Schalek, J. A. Conchello, S. Knowles-Barley, D. Lee, A. Vázquez-Reina, V. Kaynig, T. R. Jones, M. Roberts, J. L. Morgan, J. C. Tapia, H. S. Seung, W. G. Roncal, J. T. Vogelstein, R. Burns, D. L. Sussman, C. E. Priebe, H. Pfister, and J. W. Lichtman. Saturated reconstruction of a volume of neocortex. *Cell*, 162(3):648–661, July 2015.
- [29] H. Ding, R. G. Smith, A. Poleg-Polsky, J. S. Diamond, and K. L. Briggman. Species-specific wiring for direction selectivity in the mammalian retina. *Nature*, 535(7610):105–110, July 2016.
- [30] P. Arbelaez, M. Maire, C. Fowlkes, and J. Malik. Contour detection and hierarchical image segmentation. *IEEE Trans. Pattern Anal. Mach. Intell.*, pages 1–20, August 2010.
- [31] M. C. Mozer. Induction of multiscale temporal structure. In J. E. Moody, S. J. Hanson, and R. P. Lippmann, editors, *Advances in Neural Information Processing Systems 4*, pages 275–282. Morgan-Kaufmann, 1992.
- [32] A. Graves, S. Fernandez, and J. Schmidhuber. Multi-Dimensional recurrent neural networks. May 2007.
- [33] M. Liang and X. Hu. Recurrent convolutional neural network for object recognition. In *2015 IEEE Conference on Computer Vision and Pattern Recognition (CVPR)*, pages 3367–3375. IEEE Computer Society, June 2015.
- [34] J. Kim, J. K. Lee, and K. M. Lee. Deeply-Recursive convolutional network for image Super-Resolution. In *2016 IEEE Conference on Computer Vision and Pattern Recognition (CVPR)*, pages 1637–1645. IEEE, June 2016.
- [35] C. J. Sporer, P. McClure, and N. Kriegeskorte. Recurrent convolutional neural networks: A better model of biological object recognition. *Front. Psychol.*, 8:1551, September 2017.
- [36] A. R. Zamir, T.-L. Wu, L. Sun, W. Shen, J. Malik, and S. Savarese. Feedback networks. December 2016.
- [37] D. Linsley, J. K. Kim, V. Veerabadrán, C. Windolf, and T. Serre. Learning long-range spatial dependencies with horizontal gated recurrent units. In *Neural Information Processing Systems (NIPS)*, 2018.
- [38] D. A. Mély, D. Linsley, and T. Serre. Complementary surrounds explain diverse contextual phenomena across visual modalities. *Psychol. Rev.*, 125(5):769–784, October 2018.
- [39] K. Cho, B. van Merriënboer, C. Gulcehre, D. Bahdanau, F. Bougares, H. Schwenk, and Y. Bengio. Learning phrase representations using RNN Encoder–Decoder for statistical machine translation. In *Proceedings of the 2014 Conference on Empirical Methods in Natural Language Processing (EMNLP)*, pages 1724–1734, Stroudsburg, PA, USA, 2014. Association for Computational Linguistics.
- [40] M. Z. Alom, M. Hasan, C. Yakopcic, T. M. Taha, and V. K. Asari. Recurrent residual convolutional neural network based on U-Net (R2U-Net) for medical image segmentation. February 2018.
- [41] W. Shen, B. Wang, Y. Jiang, Y. Wang, and A. Yuille. Multi-stage multi-recursive-input fully convolutional networks for neuronal boundary detection. March 2017.
- [42] J. Chen, L. Yang, Y. Zhang, M. Alber, and D. Z. Chen. Combining fully convolutional and recurrent neural networks for 3D biomedical image segmentation. In D. D. Lee, M. Sugiyama, U. V. Luxburg, I. Guyon, and R. Garnett, editors, *Advances in Neural Information Processing Systems 29*, pages 3036–3044. Curran Associates, Inc., 2016.
- [43] J. Cai, L. Lu, Y. Xie, F. Xing, and L. Yang. Improving deep pancreas segmentation in CT and MRI images via recurrent neural contextual learning and direct loss function. July 2017.
- [44] R. H. Hahnloser, R. Sarpeshkar, M. a. Mahowald, R. J. Douglas, and H. S. Seung. Digital selection and analogue amplification coexist in a cortex-inspired silicon circuit. *Nature*, 405(6789):947–951, June 2000.

- [45] D. Ulyanov, A. Vedaldi, and V. Lempitsky. Instance normalization: The missing ingredient for fast stylization. July 2016.
- [46] T. Coijmans, N. Ballas, C. Laurent, Ç. Gülçehre, and A. Courville. Recurrent batch normalization. In *International Conference on Learning Representations*, 2017.
- [47] D. P. Kingma and J. Ba. Adam: A method for stochastic optimization. December 2014.
- [48] J. He, S. Zhang, M. Yang, Y. Shan, and T. Huang. Bi-Directional cascade network for perceptual edge detection. February 2019.
- [49] D. Martin, C. Fowlkes, D. Tal, and J. Malik. A database of human segmented natural images and its application to evaluating segmentation algorithms and measuring ecological statistics. In *Proceedings Eighth IEEE International Conference on Computer Vision. ICCV 2001*, volume 2, pages 416–423 vol.2, July 2001.
- [50] J. Heck and F. M. Salem. Simplified minimal gated unit variations for recurrent neural networks. January 2017.
- [51] B. O’Toole and P. Wenderoth. The tilt illusion: repulsion and attraction effects in the oblique meridian. *Vision Res.*, 17(3):367–374, 1977.
- [52] P. R. Roelfsema and R. Houtkamp. Incremental grouping of image elements in vision. *Atten. Percept. Psychophys.*, 73(8):2542–2572, November 2011.
- [53] D. A. Mély, D. Linsley, and T. Serre. Complementary surrounds explain diverse contextual phenomena across visual modalities. *Psychol. Rev.*, 2018.
- [54] M. Januszewski and V. Jain. Segmentation-Enhanced CycleGAN. February 2019.
- [55] E. Vorontsov, C. Trabelsi, S. Kadoury, and C. Pal. On orthogonality and learning recurrent networks with long term dependencies. January 2017.
- [56] J. Hu, L. Shen, S. Albanie, G. Sun, and E. Wu. Squeeze-and-Excitation networks. September 2017.
- [57] D. Linsley, D. Shiebler, S. Eberhardt, and T. Serre. Learning what and where to attend. 2019.
- [58] C. Tallec and Y. Ollivier. Can recurrent neural networks warp time? March 2018.
- [59] J. Nunez-Iglesias, R. Kennedy, T. Parag, J. Shi, and D. B. Chklovskii. Machine learning of hierarchical clustering to segment 2D and 3D images. *PLoS One*, 8(8):e71715, August 2013.
- [60] D. P. Kingma and J. Ba. Adam: A method for stochastic optimization. December 2014.
- [61] A. L. Eberle, S. Mikula, R. Schalek, J. Lichtman, M. L. Knothe Tate, and D. Zeidler. High-resolution, high-throughput imaging with a multibeam scanning electron microscope. *J. Microsc.*, 259(2):114–120, August 2015.

# Supplementary Material

## $\gamma$ -Net

The  $\gamma$ -Net is a highly recurrent extension of the U-Net for dense image prediction. Our general approach was to begin with a state-of-the-art model for dense-prediction, and then transform it (or a slightly modified version) into a gammanet by incorporating fGRU recurrent modules. For cell membrane prediction in connectomics, we build off of the U-Net of [2]. For object contour detection in natural images (BSDS500 [49]), we begin with a VGG16 pre-trained on ILSVRC12 (as with the state-of-the-art BDCN of [48]). The connectomics  $\gamma$ -Net is described in Table 5, and the BSDS  $\gamma$ -Net is described in Table 5. Beyond these differences in basic scaffold, the two implementations are distinct only in the kernel size used in their horizontal connection-learning fGRUs.

Because the current standard for computer vision applications in connectomics is to train and test on separate partitions of the same tissue volume [54], it is difficult to develop new model architectures without overfitting to any particular dataset. For this reason, we first created a synthetic dataset of cell images on which we tuned our model and explored hyperparameter choices. See Section 5 for a description of synthetic dataset generation and exemplars. With this approach, we optimized top-down/horizontal kernel sizes for the connectomics  $\gamma$ -Net and measured the influence of timesteps on performance (Fig. 5a). All models use  $1 \times 1$  top-down kernels (i.e., pointwise convolutions which do not spatially propagate of activity); horizontal kernel size is different in every layer of the connectomics  $\gamma$ -Net, but fixed at  $3 \times 3$  in the BSDS  $\gamma$ -Net (to match bottom-up kernel sizes).

In our experiments on synthetic data, we noted monotonically improved performance with increasing timesteps, which motivated our choice of building these models with as many timesteps as could fit into GPU memory without sacrificing elements from their motivating scaffolds (i.e., we did not want to distort the VGG16 architecture for the sake of increasing timesteps). We therefore settled on 8 timesteps for our models. We also compared our use of fGRU modules to learn recurrent connection vs. the classic LSTM and GRU recurrent modules, and found that the  $\gamma$ -Net was far more effective on small datasets, which we take as evidence that its recurrent application of inhibition separately from excitation is a better inductive bias for learning contour tasks (see [44] for a theoretical discussion on how these operations can amount to a digital selection of task-relevant features through inhibition, followed by an analog amplification of the residuals through excitation).

We found that model training on cell membrane detection was improved when every bottom-up unit (from a typical convolution) was given a hidden state. Like with gated recurrent architectures, these gates mean that gradients can effectively skip timesteps of processing in which there is a pathological decay. We do this by converting every convolutional layer into a “minimal gated unit” [50] (i.e., the convolutions in the first and last blocks of 5 are vanilla convolutions). This involved introducing two additional kernels,  $W^F, W^H \in \mathbb{R}^{1 \times 1 \times K \times K}$ , where the former was responsible for selecting channels from a persistent activity  $\mathbf{B} \in \mathbb{R}^{H \times W \times K}$  for processing on a given timestep as well as updating this activity. The latter kernel mapped a modulated version of the hidden state  $\mathbf{B}$  for mixing with a the vanilla convolutional activity at the layer,  $\mathbf{A} \in \mathbb{R}^{H \times W \times K}$  (see Eq 2 for the treatment). Weights in these layers were initialized with orthogonal random initializations, which are effective for training recurrent networks [55].

$$\begin{aligned} \mathbf{F} &= \sigma(\mathbf{A} + W^F * \mathbf{B}[t-1] + \mathbf{b}_F) \\ \mathbf{B}[t] &= \mathbf{F} \odot \mathbf{B}[t-1] + (1 - \mathbf{F}) \odot \text{ELU}(\mathbf{A} + W^H * (\mathbf{F} \odot \mathbf{B}[t-1]) + \mathbf{b}_H) \end{aligned} \quad (2)$$

**fGRU** Here we describe additional details on the fGRU module that we use in our experiments. Like in the original hGRU implimentation of [37], we all fGRU kernels for computing inhibitory and excitatory interactions have symmetric weights between channels. This means that the weight  $W_{x_0+\Delta x, y_0+\Delta y, k_1, k_2}$  is equal to the weight  $W_{x_0+\Delta x, y_0+\Delta y, k_2, k_1}$ , where  $x_0$  and  $y_0$  denote kernel center. This constraint means that there are nearly half as many learnable connections as a normal convolutional kernel. In our experiments, this constraint always improved performance.



Connectomics $\gamma$ -Net (450K parameters)		
Layer	Operation	Output shape
conv-1-down	conv $3 \times 3 / 1$	$384 \times 384 \times 24$
	conv $3 \times 3 / 1$	$384 \times 384 \times 24$
	fGRU-horizontal $9 \times 9 / 1$	$384 \times 384 \times 24$
	maxpool $2 \times 2 / 2$	$192 \times 192 \times 24$
conv-2-down	conv $3 \times 3 / 1$	$192 \times 192 \times 28$
	fGRU-horizontal $7 \times 7 / 1$	$192 \times 192 \times 28$
	maxpool $2 \times 2 / 2$	$96 \times 96 \times 28$
conv-3-down	conv $3 \times 3 / 1$	$96 \times 96 \times 36$
	fGRU-horizontal $5 \times 5 / 1$	$96 \times 96 \times 36$
	maxpool $2 \times 2 / 2$	$48 \times 48 \times 36$
conv-4-down	conv $3 \times 3 / 1$	$48 \times 48 \times 48$
	fGRU-horizontal $3 \times 3 / 1$	$48 \times 48 \times 48$
	maxpool $2 \times 2 / 2$	$24 \times 24 \times 48$
conv-5-down	conv $3 \times 3 / 1$	$24 \times 24 \times 64$
	fGRU-horizontal $1 \times 1 / 1$	$24 \times 24 \times 64$
conv-4-up	transpose-conv $4 \times 4 / 2$	$48 \times 48 \times 48$
	conv $3 \times 3 / 1$	$48 \times 48 \times 48$
	instance-norm	$48 \times 48 \times 48$
	fGRU-top-down $1 \times 1 / 1$	$48 \times 48 \times 48$
conv-3-up	transpose-conv $4 \times 4 / 2$	$96 \times 96 \times 36$
	conv $3 \times 3 / 1$	$96 \times 96 \times 36$
	instance-norm	$96 \times 96 \times 36$
	fGRU-top-down $1 \times 1 / 1$	$96 \times 96 \times 36$
conv-2-up	transpose-conv $4 \times 4 / 2$	$192 \times 192 \times 28$
	conv $3 \times 3 / 1$	$192 \times 192 \times 28$
	instance-norm	$192 \times 192 \times 28$
	fGRU-top-down $1 \times 1 / 1$	$192 \times 192 \times 28$
conv-1-up	transpose-conv $4 \times 4 / 2$	$384 \times 384 \times 24$
	conv $3 \times 3 / 1$	$384 \times 384 \times 24$
	instance-norm	$384 \times 384 \times 24$
	fGRU-top-down $1 \times 1 / 1$	$384 \times 384 \times 24$
Readout	instance-norm	$384 \times 384 \times 24$
	conv $5 \times 5 / 1$	$384 \times 384 \times 24$

Table S1:  $\gamma$ -Net specification for cell membrane detection in SEM images. Down refers to down-sampling layers; up refers to up-sampling layers, and readout maps model activities into per-pixel decisions. Kernels are described as kernel-height  $\times$  kernel-width / stride size. All fGRU non-linearities are linear rectifications, and all convolutional non-linearities are exponential linear units (ELU), as in [2].

BSDS (20M parameters) $\gamma$ -Net		
Layer	Operation	Output shape
conv-1-down	conv $3 \times 3 / 1$	$320 \times 480 \times 64$
	conv $3 \times 3 / 1$	$320 \times 480 \times 64$
	maxpool $2 \times 2 / 2$	$160 \times 240 \times 64$
conv-2-down	conv $3 \times 3 / 1$	$160 \times 240 \times 128$
	conv $3 \times 3 / 1$	$160 \times 240 \times 128$
	fGRU-horizontal $3 \times 3 / 1$	$160 \times 240 \times 128$
	maxpool $2 \times 2 / 2$	$80 \times 120 \times 128$
conv-3-down	conv $3 \times 3 / 1$	$80 \times 120 \times 256$
	conv $3 \times 3 / 1$	$80 \times 120 \times 256$
	conv $3 \times 3 / 1$	$80 \times 120 \times 256$
	fGRU-horizontal $3 \times 3 / 1$	$80 \times 120 \times 256$
	maxpool $2 \times 2 / 2$	$40 \times 60 \times 256$
conv-4-down	conv $3 \times 3 / 1$	$40 \times 60 \times 512$
	conv $3 \times 3 / 1$	$40 \times 60 \times 512$
	conv $3 \times 3 / 1$	$40 \times 60 \times 512$
	fGRU-horizontal $3 \times 3 / 1$	$40 \times 60 \times 512$
	maxpool $2 \times 2 / 2$	$20 \times 30 \times 512$
conv-5-down	conv $3 \times 3 / 1$	$20 \times 30 \times 512$
	conv $3 \times 3 / 1$	$20 \times 30 \times 512$
	conv $3 \times 3 / 1$	$20 \times 30 \times 512$
	fGRU-horizontal $3 \times 3 / 1$	$20 \times 30 \times 512$
conv-4-up	instance-norm	$20 \times 30 \times 512$
	bilinear-resize	$40 \times 60 \times 512$
	conv $1 \times 1 / 1$	$40 \times 60 \times 8$
	conv $1 \times 1 / 1$	$40 \times 60 \times 512$
	fGRU-top-down $1 \times 1 / 1$	$40 \times 60 \times 512$
conv-3-up	instance-norm	$40 \times 60 \times 512$
	bilinear-resize	$80 \times 120 \times 512$
	conv $1 \times 1 / 1$	$80 \times 120 \times 16$
	conv $1 \times 1 / 1$	$80 \times 120 \times 256$
	fGRU-top-down $1 \times 1 / 1$	$80 \times 120 \times 256$
conv-2-up	instance-norm	$80 \times 120 \times 256$
	bilinear-resize	$160 \times 240 \times 256$
	conv $1 \times 1 / 1$	$160 \times 240 \times 64$
	conv $1 \times 1 / 1$	$160 \times 240 \times 128$
	fGRU-top-down $1 \times 1 / 1$	$160 \times 240 \times 128$
Readout	instance-norm	$160 \times 240 \times 128$
	bilinear-resize	$320 \times 480 \times 128$
	conv $1 \times 1 / 1$	$320 \times 480 \times 1$

Table S2:  $\gamma$ -Net specification for contour detection in BSDS natural images. Down refers to down-sampling layers; up refers to up-sampling layers, and readout maps model activities into per-pixel decisions. Kernels are described as kernel-height  $\times$  kernel-width / stride size. All non-linearities in this network are linear rectifications.

While optimizing on our synthetic datasets, we found that a small modification of the fGRU input gate offered a modest improvement in performance. We realized that the construction of the input gate in the fGRU is conceptually similar to recently developed models for bottom-up attention in deep neural networks. Specifically, the squeeze-and-excitation networks of [56], and global-and-local attention modules of [57], in which a non-linear transformation of a layer’s activity is used to modulate it. Here, we took inspiration from global-and-local attention, and introduced an additional gate into the fGRU, resulting in the following modification of the main equations.

$$\begin{aligned}
\mathbf{G}^{IG} &= U^{IG} * \mathbf{H}[t-1] \\
\mathbf{G}^{IS} &= U^{IS} * \mathbf{H}[t-1] \\
\mathbf{G}^I &= \sigma(\text{IN}(\mathbf{G}^{IG} \odot \mathbf{G}^{IS*})) \\
\mathbf{C}^I &= \text{IN}(W^I * (\mathbf{H}[t-1] \odot \mathbf{G}^I)) \\
\mathbf{Z} &= \left[ \mathbf{X} - \left[ (\alpha \mathbf{H}[t-1] + \mu) \mathbf{C}^I \right]_+ \right]_+ \\
\mathbf{G}^E &= \sigma(\text{IN}(U^E * \mathbf{Z})) \\
\mathbf{C}^E &= \text{IN}(W^E * \mathbf{Z}) \\
\tilde{\mathbf{H}} &= \left[ \kappa(\mathbf{C}^E + \mathbf{Z}) + \omega(\mathbf{C}^E * \mathbf{Z}) \right]_+ \\
\mathbf{H}[t] &= (1 - \mathbf{G}^E) \odot \mathbf{H}[t-1] + \mathbf{G}^E \odot \tilde{\mathbf{H}}
\end{aligned} \tag{3}$$

where  $\text{IN}(\mathbf{r}; \delta, \nu) = \nu + \delta \odot \frac{\mathbf{r} - \widehat{\mathbb{E}}[\mathbf{r}]}{\sqrt{\widehat{\text{Var}}[\mathbf{r}] + \eta}}$ .

We thus introduce “global” and “local” gates  $\mathbf{G}^{IG}, \mathbf{G}^{IS} \in \mathbb{R}^{W \times H \times K}$ , which are computed as filter responses between the previous hidden state  $\mathbf{H}[t-1]$  with the global filter  $U^{IG} \in \mathbb{R}^{1 \times 1 \times K \times K}$  and the local filter  $U^{IS} \in \mathbb{R}^{3 \times 3 \times K \times I}$ . Note that the latter filter is learning a mapping into 1 dimension and is therefore first tiled into  $K$  dimensions before elementwise multiplication with  $\mathbf{G}^{IG}$ . All results in the main text use this implementation since it led to a minor improvement in performance on our synthetic cell membrane detection tasks.

Following the lead of [37], we incorporated normalizations into the fGRU. Let  $\mathbf{r} \in \mathbb{R}^d$  denote the vector of layer activations that will be normalized. We chose instance normalization [45], since it is independent of batch size, which were 1 in our experiments. Instance normalization introduces two  $k$ -dimensional learned parameters,  $\delta, \nu \in \mathbb{R}^d$  control the scale and bias of normalized activities, and are shared across timesteps of processing. In contrast, means and variances are computed on every timestep, so that the normalization does not constrain fGRU dynamics. Elementwise multiplication is denoted by  $\odot$  and  $\eta$  is a regularization hyperparameter.

Learnable gates, such as those in the fGRU, are helpful for training RNNs. But there are a variety of other heuristics that are also important for optimizing performance. We use several of these to when training  $\gamma$ -Nets, such as Chronos initialization of fGRU gate biases [58] and random orthogonal initialization of model weights [55]. We additionally initialized the learnable scale parameter  $\delta$  of fGRU normalizations to 0.1, since values near 0 optimize the dynamic range of gradients passing through its sigmoidal gates [46]. Similarly, fGRU parameters for learning additive inhibition/excitation ( $\mu, \kappa$ ) were initialized to 0, and parameters for learning multiplicative inhibition/excitation ( $\alpha, \omega$ ) were initialized to 0.1. Finally, when implementing top-down connections, we incorporated an extra skip connection, which we found improved the stability of training. Consider the horizontal activities in two layers,  $\mathbf{H}^{(l)}, \mathbf{H}^{(l+1)}$ , and the function fGRU described in the main text, which implements top down connections. Top-down connections introduce a skip connection to this function, resulting in:  $\mathbf{H}^{(l)} = \text{fGRU}(\mathbf{H}^{(l)}, \mathbf{H}^{(l+1)}) + \mathbf{H}^{(l)}$ .

## Membrane prediction models

Our reference model for membrane prediction is the 3D U-Net of [2]. We followed their published routine for validating our implementation of their U-Net model.

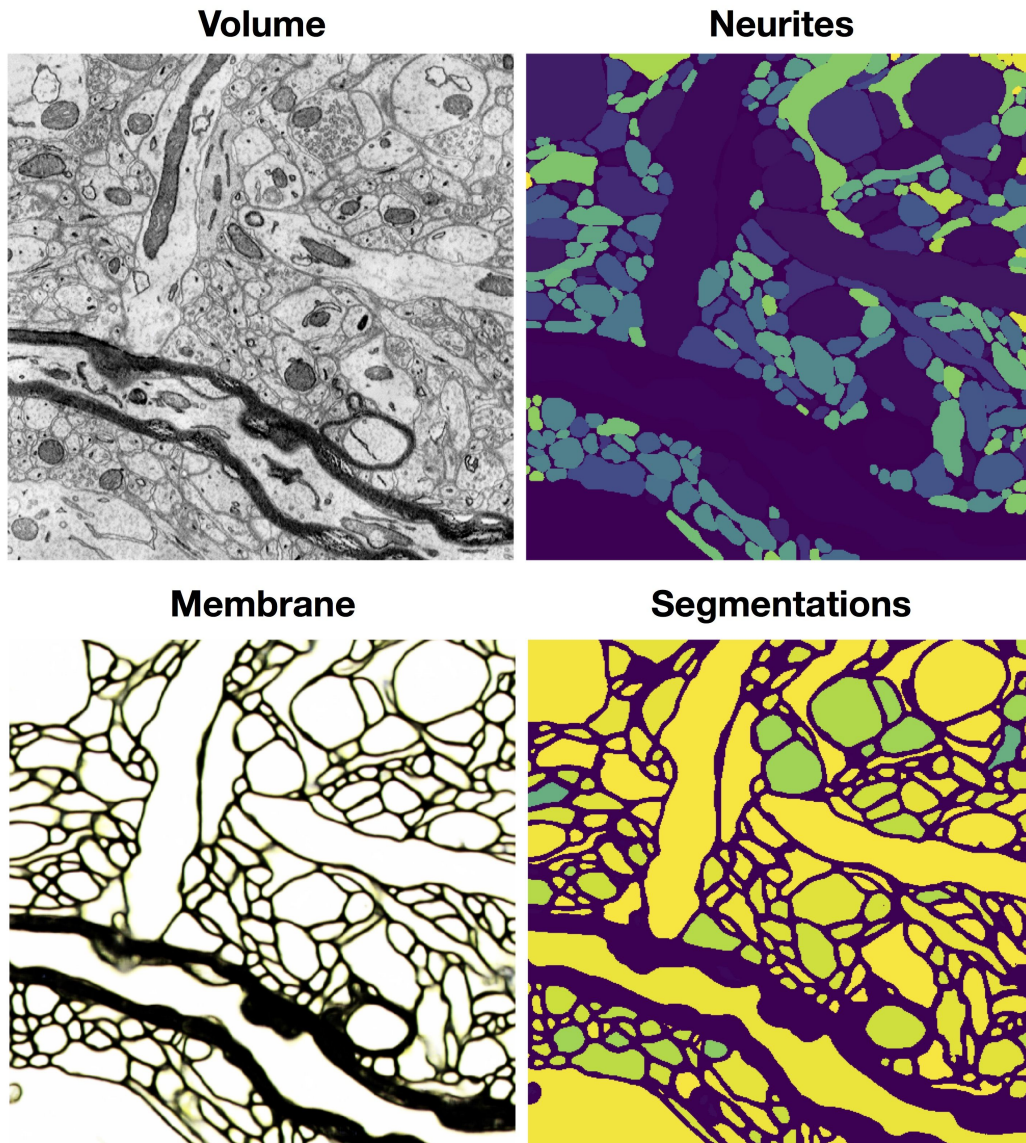


Figure S1: We trained the reference 3D U-Net from [2] on the SNEMI3D dataset to validate the implementation. Segmentations here are derived by watershedding and agglomeration with GALA [59], resulting in “superhuman” ARAND (evaluated according to the SNEMI3D standard; lower is better) of 0.04, which is below the reported human-performance threshold of 0.06 and on par with the published result (see Table 1 in [2], mean affinity agglomeration).

Name	Tissue	Imaging	Resolution	Voxels (X/Y/Z/Volumes)
SNEMI3D [28]	Mouse cortex	mbSEM [61]	$6 \times 6 \times 29\text{nm}$	$1024 \times 1024 \times 100 \times 1$
Ding [29] (Ours)	Mouse retina	SBEM [29]	$13.2 \times 13.2 \times 26\text{nm}$	$384 \times 384 \times 384 \times 1$

Table S3: SEM image volumes used in membrane prediction. SNEMI3D images and annotations are publicly available, whereas the Ding dataset is a volume from [29] annotated by us.

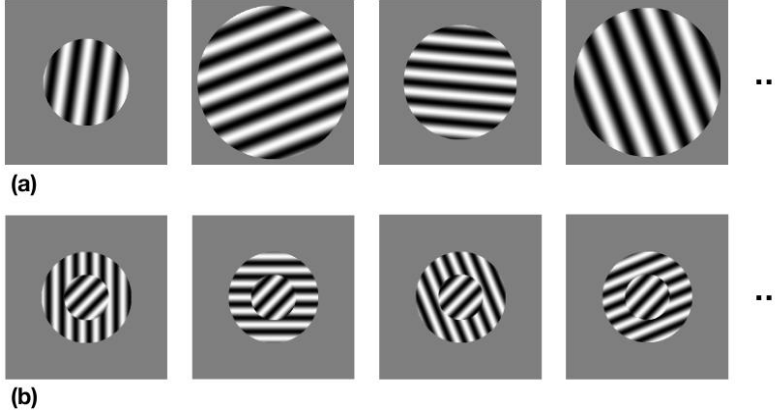


Figure S2: Examples of tilt-illusion stimuli. **(a)** For training images, we sample over a range of size and wavelength to generate single oriented grating patches. **(b)** Test images are obtained by sampling a full range of surround orientation, while fixing all other parameters such as size and frequency of gratings as well as the orientation of the center gratings (at 45 degrees).

Key to this is their use of a large set of random data augmentations applied to SEM image volumes, which simulate common noise and errors in SEM imaging. These are (i) misalignment between consecutive  $z$ -locations in each input image volume. (ii) Partial- or fully-missing sections of the input image volumes. (iii) Blurring of portions of the image volume. Augmentations that simulated these types of noise, as well as random flips over the  $xyz$ -plane, rotations by  $90^\circ$ , brightness and contrast perturbations, were applied to volumes following the settings of [2]. The model was trained using Adam [60] and the learning rate schedule of [2], in which the optimizer step-size was halved when validation loss stopped decreasing (up to four times). Training involved single-SEM volume batches of  $160 \times 160 \times 18$  (X/Y/Z), normalized to  $[0, 1]$ . As in [2], models were trained to predict nearest-neighbor voxel affinities, as well as 3 other mid- to long-range voxel distances, as in [2]. Only the nearest neighbors were used at test time.

### Tilt illusion image dataset

Models were tested for a tilt illusion by first training on grating images of a single orientation, then testing on images in which a center grating had the same/different orientation as a surround grating. Each image in the training dataset consisted of a circular patch of oriented grating on a gray canvas of size  $500 \times 500$  pixels. To ensure that the decoder successfully decoded orientation information from model activities, the training dataset incorporated a wide variety of grating stimuli with 4 randomly sampled image parameters:  $r$ ,  $\lambda$ ,  $\theta$ , and  $\phi$ .  $r$  denotes the radius of the circle in which oriented grating has been rendered, and was sampled from a uniform distribution with interval between 80 and 240 pixels;  $\lambda$  specifies the wavelength of the grating pattern and was sampled from a uniform distribution with interval between 30 and 90 pixels;  $\theta$  specifies the orientation of the gratings and is uniformly sampled from all possible orientations;  $\phi$  denotes the phase offset of the oriented gratings and is also uniformly sampled from all possible values. The models' BSDS-trained weights were fixed and their readout layers (described in the main text) were trained to decode orientation at the center of each image. This setup allowed us to tease apart the effects of the surround on the representation of orientation in the center by introducing separate surround regions in each test image filled with gratings with same/different orientations as the center (Fig.5b). Each test image was generated



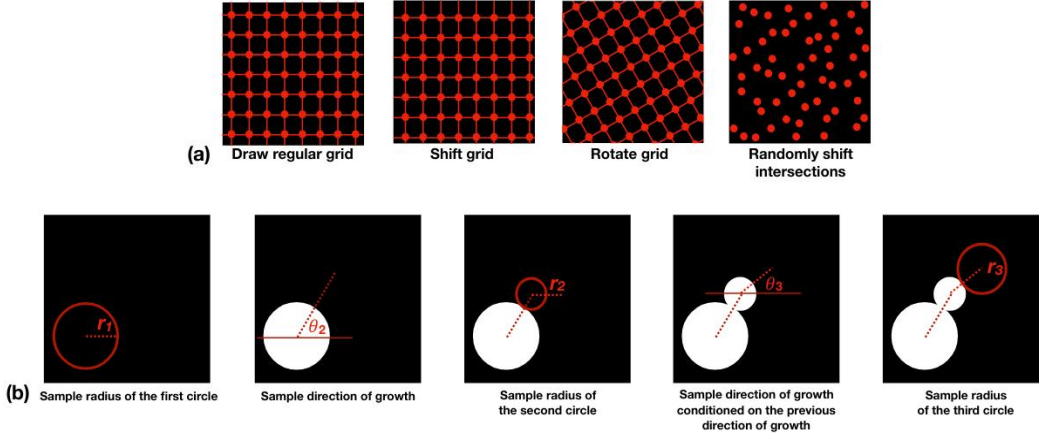


Figure S3: A visual depiction of the cell-skeleton generation algorithm. **(a)** Image generation starts by first sampling the candidate seed positions for cell skeletons. A regular grid is generated and undergoes random shift, rotation and random, independent perturbation of its intersections. **(b)** Depiction of cell-skeleton generation procedure. A cell skeleton is modeled as a chain of filled circles that are serially attached in random orientations.

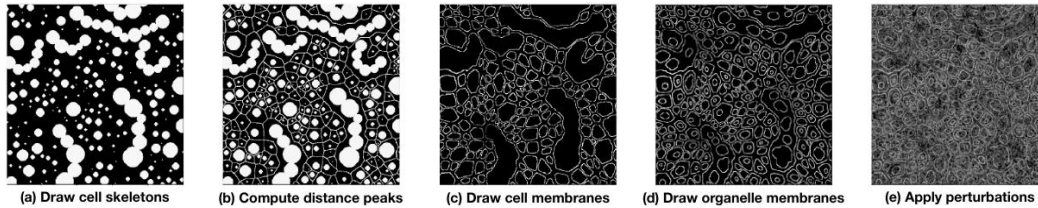


Figure S4: A visual depiction of the membrane image generation procedure.

with one additional parameter,  $\Delta\theta$  which specified orientation difference of the surround gratings with respect to the center orientation,  $\theta$ , and was sampled from a uniform distribution with interval between  $-90$  and  $+90$  degrees. The radius of the surround grating is denoted by  $r$  and was sampled from the same uniform distribution we used in training dataset. Center gratings are then rendered in a circle of radius that is one half of the surround gratings.

## Synthetic Connectomics Challenge

**Overview** The main goal of the Synthetic Connectomics Challenge is to investigate machine vision systems' ability in detecting cell membranes in noisy tissue images. The challenge consists of randomly generated synthetic, noisy images of cell membranes and organelles. The task goal is to emit per-pixel predictions of cell membranes (1s at membranes and 0s everywhere else). By gradually reducing the number of training images allowed to train a model on, we systematically investigate if a system can generalize to test images by inducing the principles of cell boundary detection (e.g., gestalt principles of good continuity and containment) based on a small number of training examples.

Each image in our challenge consists of multiple cell membranes, which are randomly shaped closed curves. Different cell membranes never touch or intersect with each other; as a result, cell membranes topologically partition an image into either intracellular space (soma) or extracellular space. Some cells may contain an arbitrary number of closed curves inside its intracellular space; these curves represent organelle membranes. Similar to cell membranes, organelle membranes never intersect or overlap with each other. As a result, organelle membranes further partition the interior space of each cell to soma and organelle. Because cell and organelle membranes are rendered with curves of identical thickness and luminance, they are locally indistinguishable. The only reliable visual cue that distinguishes cell membranes from organelle membranes is a topological one – whether or not a given membrane is contained inside another membrane. Thus, the main task in this challenge is

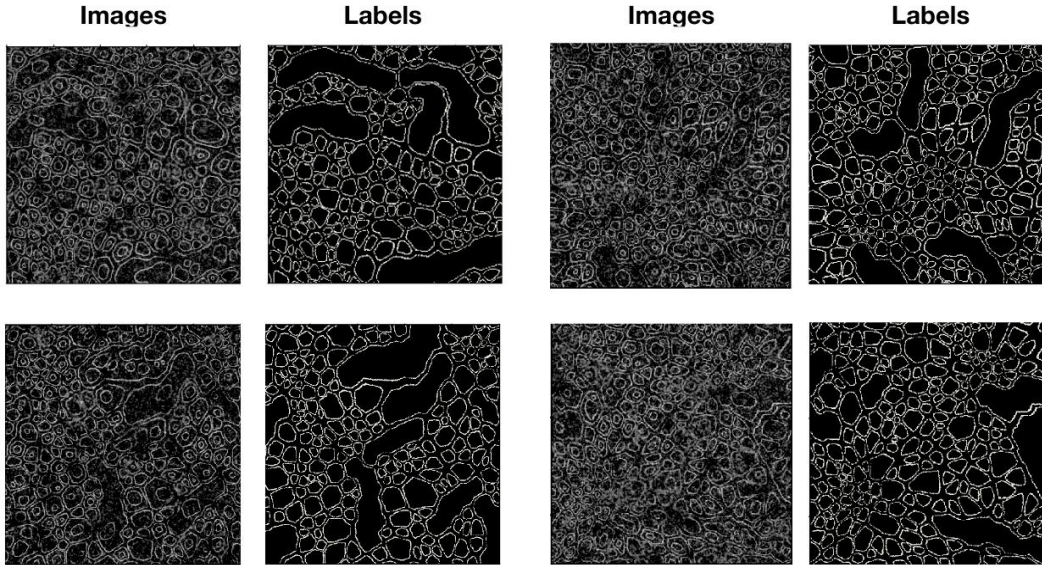


Figure S5: Four example images of the synthetic connectomics challenge paired with ground-truth cell membrane images.

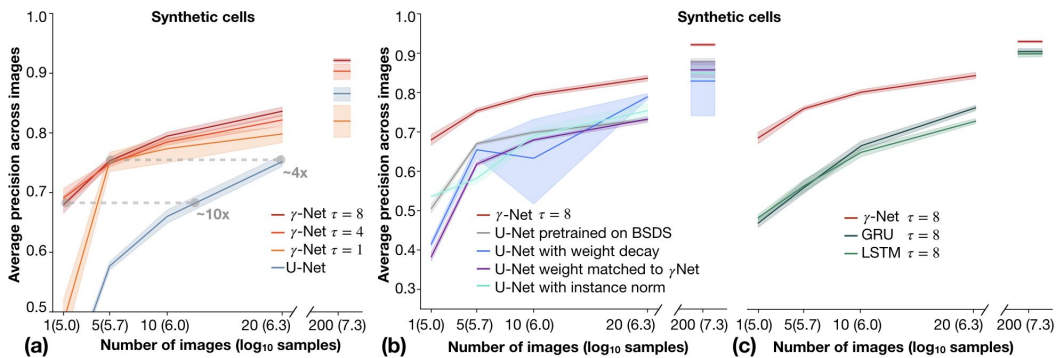


Figure S6:  $\gamma$ -Net hyperparameter survey and comparison with other recurrent models. We show model results on our synthetic membrane detection challenge when trained on a proportion of the total dataset. Results are reported as the mean of average precisions across the same synthetic cell test set. (a)  $\gamma$ -Net performance monotonically improves with timesteps of processing. Grey markers show that the U-Net of [2] needs far more samples to reach similar performance as the  $\gamma$ -Net. (b) Comparisons between the 8-timestep  $\gamma$ -Net and control specifications of the U-Net. (c) The  $\gamma$ -Net is more effective when its recurrence is controlled with fGRUs vs. a GRU or LSTM.

to detect topological cues that distinguish cells from organelles, in addition to solving other image processing problems such as de-noising and de-blurring.

One of the main inspirations behind the design of the image generator is the idea that membrane morphology is determined by mechanical balance between pressures applied between intracellular cytoskeletons. We distill this idea into a simplified image generation algorithm in which cell (and organelle) membranes are generated based on what we call ‘skeletons’ – solid shapes which represent a backbone of each cell or organelle. Then, the shape and positions of cell membranes between two adjacent cells are determined by the shape and relative spatial arrangement of the two cells’ skeletons (Fig. S4c).

**Positioning skeletons** The first step of image generation algorithm involves sampling the positions of cytoskeletons in an image. A regular square grid of side length 15 is rendered on a 500 by 500 image. A set of candidate locations are defined as intersects on the grid. The generation algorithm loops through these locations, randomly shifting each location by a displacement vector sampled

from a uniform distribution over a solid circle of radius of 50. Should a random displacement cause two candidate locations to overlap, the current candidate location is rejected. The algorithm then renders a skeleton on each candidate location (Fig. S3a).

**Generating single-circle skeletons** For simplicity, we use solid circles as cell skeletons for the majority of cells in each image. We call these skeletons “single-circle skeletons”. In each candidate location, a single-circle skeleton is rendered with a randomly sampled radius. The radius of a single skeleton is sampled from a normal distribution with mean 10 and standard deviation 15 (with its negative-side tail truncated at 2 and the positive side at two standard deviations away from the mean). In all cases, cell skeletons from different cells are prevented from touching or overlapping using rejection sampling.

**Snake-like skeletons** To render large, extended cells, we allow some cells to have what we call “snake-like skeletons”. Snake-like skeletons are multiple solid circles that are linearly chained together to form an elongated shape. Similar to single-circle skeletons, the first circle is sampled and rendered with its center at each candidate position. Next, additional circles are sequentially added so that the circles form a snake-like chain. For clarity, we call the most recently added circle the “tail circle”. While growing a snake-like skeleton, each new circle is positioned so that it lightly overlaps with the tail circle. This is ensured by placing the center of a new circle at a distance from the center of the tail circle that is 2 pixels fewer than the sum of the radii of the two touching circles. This process is depicted in Fig. S3b.

The direction in which each snake-like skeleton grows is determined by the orientation of the line formed between the centers of each new circle and each tail circle. The orientation is sampled from a probability distribution specified by the difference between angle formed between the line that connects the centers of the current tail circle and the new circle and the line that connects the centers of the tail circle and the previous tail circle,  $\Delta\theta = \theta_i - \theta_{i-1}$ :

$$P(\theta_i) = \frac{1}{Z} \max(\cos(c\Delta\theta), 0) \quad (4)$$

$$\text{where } Z = \int_{-\frac{\pi}{2}}^{\frac{\pi}{2}} \cos(\theta) d\theta = 2 \quad (5)$$

Note that we use a continuity parameter  $c$  that constrains the possible range of a turn each new trailing circle can make. This parameter determines the overall rigidity of the direction in which a snake-like skeleton grows. We fix its value at 1.2. Using rejection sampling, we additionally ensure that the growing skeleton never touches itself to form a loop.

In each image, 18 snake-like skeletons are sampled – 6 “short”, 6 “moderate” and 6 “long” snake-like skeletons. They are rendered at random among candidate skeleton locations, while single-circle skeletons are rendered in the remainder of candidate locations. Each type of extended skeleton is sampled using different combinations of length parameters, which determine the number of circles that make up each snake-like skeleton. The length of short skeletons, for example, is sampled from a normal distribution of mean 3 and standard deviation of 2, truncated on the negative side at 1 and on the positive side at two standard deviations away from the mean. The length of moderate skeletons is sampled from a normal distribution of mean 4 and standard deviation of 2. For long skeletons, a normal distribution of mean 8 and standard deviation of 2.

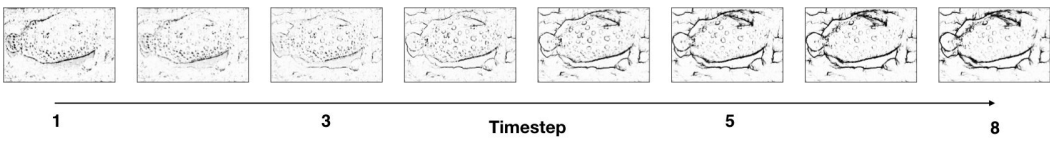
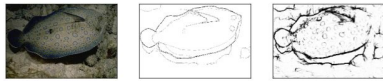
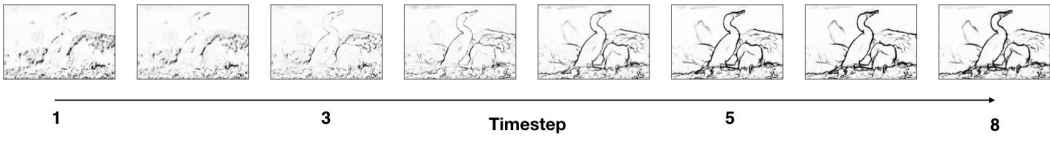
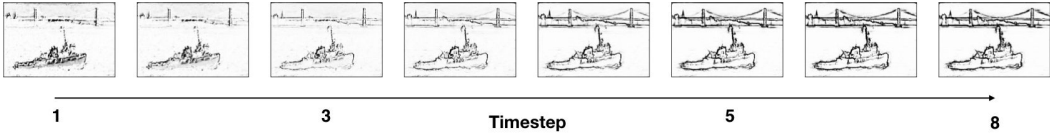
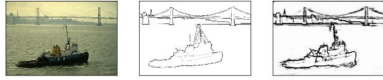
The radius of individual circles in each type of snake-like skeleton is also sampled using different parameters. In long snake-like skeletons, the radius of each circle is sampled from a normal distribution with mean of 30 and standard deviation of 6, truncated at two standard deviations away. Circle radius in moderate snake-like skeletons is sampled with mean of 40 and standard deviation of 8. In short skeletons, we use mean of 10 and standard deviation of 15.

**Rendering cell membranes** Once all cell skeletons have been rendered, a distance transform to the skeleton image finds a collection of local distance maxima from nearest skeletons. These pixels are added back to the skeleton image, and then another distance transform is applied. We use the resulting peak points as cell membranes.

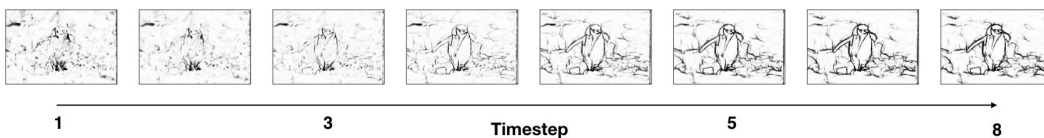
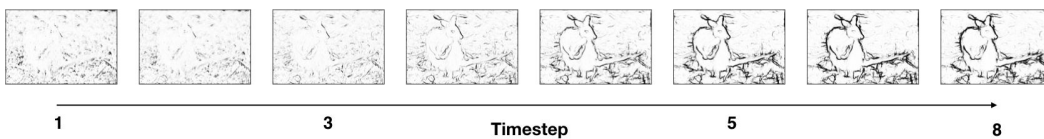
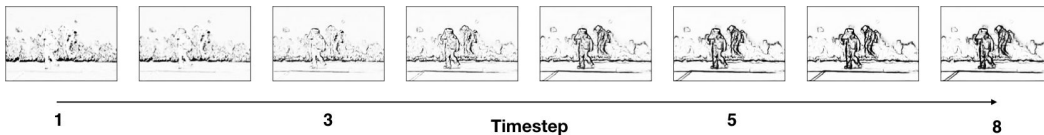
**Rendering organelle membranes** Organelle membranes are sampled and rendered in a similar way to cell membranes. Here, the algorithm loops through each cell and, with probability of 0.5, renders organelles. Once the algorithm determines to render organelles in a cell, an arbitrary number of organelle skeletons are rendered until the total area covered by organelle skeletons in a cell occupies at least 30% of the cell's interior area. Organelle skeletons are snake-like skeletons with length sampled from a (truncated) normal distribution with mean of 3 and standard deviation of 1. The radius of individual circles that make up these skeletons is also sampled from a truncated normal distribution with mean 10 and standard deviation 15. Once skeletons have been generated, organelle membranes are also rendered via the two-step application distance transformation, similar to how cell membranes are rendered.

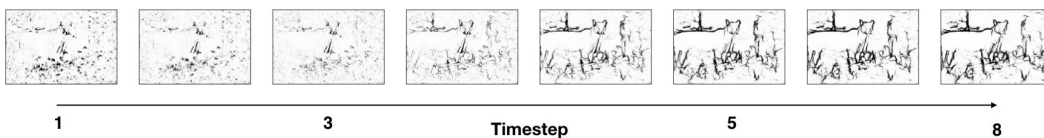
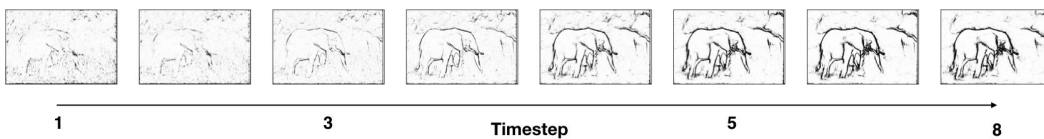
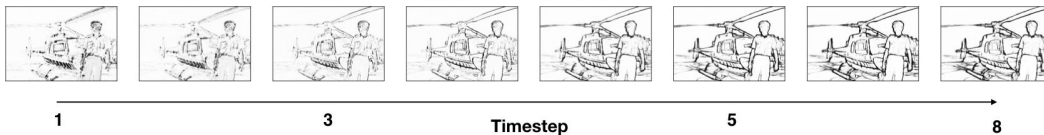
**Perturbations** Once both cell and organelle membranes have been generated, the image undergoes additional post-processing steps through which image details are purposefully destroyed. This stage consists of four processing steps: geometric warp, contrast modulation, blurring and the addition of noise. First, geometric warping is carried out by creating a 'transformation template': a grayscale image in the same shape as the membrane image. Twenty randomly positioned Gaussian bumps with a width of 20 pixels are added to the image, after which the template is normalized such that pixel values range from 0 to 1. Each pixel in the membrane image is translated by a displacement proportional to the gradient of the transformation template in the corresponding location. Next, random contrast modulation and blurring differentially suppresses contrast and blurs the image, lowering visibility of membranes. We generate two additional transformation templates for this step. During contrast modulation, contrast in each pixel in membrane image is then reduced by the rate specified by 1 minus the value of the corresponding pixel in its transformation template. Likewise, the intensity of blur applied to each pixel is determined by the value of the corresponding pixel in its transformation template. Lastly, pixel noise is added to the membrane image, sampled from a normal distribution of mean zero and standard deviation of 0.5.

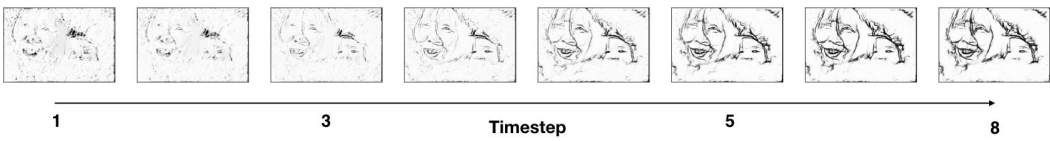
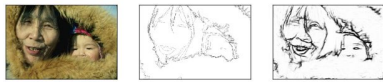
**Additional  $\gamma$ -Net predictions on BSDS**











## **Additional $\gamma$ -Net predictions on mouse retina**

